Available online at www.sciencedirect.com

ScienceDirect

Journal of Nuclear Materials 374 (2008) 20–31

journal of nuclear materials

www.elsevier.com/locate/jnucmat

Localized corrosion of 316L stainless steel in tritiated water containing aggressive radiolytic and decomposition products at different temperatures

G. Bellanger *

French Atomic Energy Commission, 10 Avenue de la Paix, F21260 Selongey, France

Received 30 December 2006; accepted 6 July 2007

Abstract

Tritium is one of the more important radionuclides used in nuclear industry as plutonium and uranium. The tritium in tritiated water always causes difficulties in nuclear installations, including equipment corrosion. Moreover, with tritiated water there are, in addition, the radiolytic and decomposition products such as hydrogen peroxide formed during decay, chloride ions produced by degradation of organic seals and oils used for tightness and pumping, and acid pH produced by excitation of nitrogen in air by the β^- particle. Highly concentrated tritiated water releases energy and its temperature is about 80 °C, moreover heating is necessary in the tritium processes. These conditions highly facilitate the corrosion of stainless steels by pitting and crevice attack. Corrosion tests were performed by electrochemical analysis methods and by visual inspection of the surface of stainless steel.

PACS: 25.55.−e; 82.45.Bb; 81.70.−q; 68.47.Gh

1. Introduction

The stainless steel used in the civilian (ITER) and military plants for the reprocessing of the tritiated water is type 316L austenitic stainless steel, which has a good corrosion resistance compared with other steels. However, several cases of corrosion have occurred in these reprocessing plants [1]. The tritium in tritiated water decays with the formation of helium and the emission of a β^- particle. The energy released (W) in this decay is 5.7 keV per tritium atom, which is high enough to locally decompose the tritiated water molecules along the path of the β^- particle. This leads to the formation of radiolytic products like hydrogen peroxide [2–4]. The reactions occurring in this decay can be summarized as follows:

$$^3\mathrm{H_2O} \rightarrow 2\,^3\mathrm{He} + 0.5\mathrm{O_2}\ _{\mathrm{dissolved}} + 2\beta^- \quad W = 5.7 \times 2\ \mathrm{keV}, \tag{1}$$

$$^3\mathrm{H_2O},\ 0.5\mathrm{O_2} + \beta^- \rightarrow \{^3\mathrm{H}^*, {}^3\mathrm{HO}_2^*\ldots\}_{\mathrm{solvated}} \rightarrow {}^3\mathrm{H_2O_2} \tag{2}$$

The solvated radicals have a very short life (lower than 10^{-7} s), reacting rapidly with other radicals, and it is difficult to know their kinetics and to show their existence. Besides, $^3H_2O_2$ is stable and can easily be analyzed and quantified. During the radiolysis of the tritiated water, finally the formation of the hydroxonium ions ($^3H_3O^+$) does not appear. Tritiated water should not be acidic in the absence of impurity.

As with water, the β^- particle energy decomposes the organic polymer joints in valves or vacuum pump oils when these are in contact with gaseous tritium or tritiated water vapor. If these polymers have R–Cl bonds, then the decomposition reaction would be

$$\mathrm{R{-}Cl} + {}^3\mathrm{H_2O} + \beta^- \rightarrow \mathrm{Cl}^- + {}^3\mathrm{H}^{+3}\mathrm{HCO_3^-} + \mathrm{R'}{-} \tag{3}$$

where R and R′ represent organic radicals. It was observed that the decomposition of sintered Ni + PTFE or PVC

---

* Tel./fax: +33 380757610.
E-mail address: gilbert.bellanger@wanadoo.fr
URL: http://corrosion.monsite.wanadoo.fr

0022-3115/$ - see front matter © 2007 Elsevier B.V. All rights reserved.
doi:10.1016/j.jnucmat.2007.07.005

composites tested in our laboratories is visible after two months and the concentrated tritiated water used (e.g., 1.5 PBq dm^{-3}) becomes brownish during decomposition. Color disappears when the composite is removed from the tritiated water. After soaking, this tritiated water contains an appreciable concentration of chloride and carbonic acid.

An acidic medium was selected since, unfortunately, relatively concentrated acid solutions are produced in tritiated water when this or tritiated vapor is in contact with air. This can be explained by the effect of β^- particles on the nitrogen in air [2–4]:

$$N_2 + \beta^- \rightarrow 2N^* \tag{4}$$

$$N^* + 3\,{}^3H_2O \rightarrow {}^3HNO_3 + 5\,{}^3H^* \tag{5}$$

Taking as an example, a tank of tritiated water at a concentration of 3 g dm^{-3} in tritium, at the atmospheric pressure was cooled at a temperature of 25 °C, and its radioactivity was 1.5 PBq dm^{-3} and the energy transferred in the tritiated water was 8 EeV $dm^{-3}\,s^{-1}$.

The gas phase contains nitrogen, oxygen, tritium and tritiated water vapor. At the pseudoequilibrium, the tritium concentration in the gas phase will be

$$\sum {}^3H = 35\ \text{nmol cm}^{-3} \tag{6}$$

and the energy released can be written as

$$dE/dt = \lambda \mathcal{N} W \Sigma {}^3H, \tag{7}$$

where t is the time, λ the disintegration constant (1.8 ns^{-1}) and $\mathcal{N}$ the Avogadro number. Formulating the hypothesis that nitrogen absorbs 80% of the energy and taking an efficiency of 2% to produce the nitric acid [2–4], the energy used and the rate of formation in acid (v) will be

$$dE/dt = 0.2\ \text{TeV cm}^{-3}\,\text{s}^{-1}, \tag{8}$$

$$v = 5\ \text{fmol cm}^{-3}\,\text{s}^{-1}. \tag{9}$$

In application, tritiated water initially at pH 7 will have a pH of 4 after one year of stocking in the presence of air. In this environment, the tritiated water becomes acidic, and contains hydrogen peroxide. This will be aggressive for corrosion. In addition, circumstances become worse, the concentration in nitric acid formed also depends on the exchange surface between the gas and liquid phases and temperature. Large surface and high temperature rapidly lead to a high concentration of tritiated vapor and the tritiated water quickly becomes very acidic.

Therefore, in this work we studied the effect of temperature on corrosion of the 316L stainless steel in tritiated water containing chloride and hydrogen peroxide at pH 4.

2. Experimental equipment and procedure

To analyze the tritiated water and to test the corrosion, it was necessary to realize a system of reliable sampling and not contaminating it for the reprocessing (avoiding to spill the tritiated water outside the metal tank or the jug for sampling). The same arrangement was made for the evacuation of the tritiated water after analysis.

The materials (Fig. 1(A) and (B)) used for the sampling are

- a safe small jug (1) made of strengthened glass resistant to shocks and accidental falls and sheathed outside with a plastic membrane. Glass is chosen to have a visual control over the level of filling,
- a supple rubber membrane (2) put in the opening of the small jug. The membrane is maintained in place by an open (3) or closed (4) screwed cork. The closed cork ensures tightness and is used to carry the tritiated water from the stocking to the 'hot' laboratory,
- a hollow needle (5) to drill the membrane and to introduce the tritiated water into the small jug, or to empty the small jug,
- a needle guide head (6) to protect the fingers of the operator against the extremity of the sharpened needle contaminated by tritiated water. The needle is in contact with the tritiated water for sampling or its recuperation after analysis.

During the process of sampling, the small jug is in depression with regard to the tank containing tritiated water to be analyzed. The necessary amount of tritiated water is sucked up in the small jug. The recovery of the tritiated water after analysis is made from the small jug at the atmospheric pressure to the metal tank in depression and where the stocked tritiated water is frozen at −40 °C. The tritiated water analyzed is sucked up in this tank.

To ensure safety, a thermostated electrochemical cell (Fig. 2) was specially constructed with a dual wall made of thick glass and put in a highly stable rigid plastic tank. In case of breakage of the glass, this arrangement has the advantage that the tritiated water is contained in this tank and is not spilled over the bottom of the glove box used for the tests. All the corrosion tests were, therefore, carried out

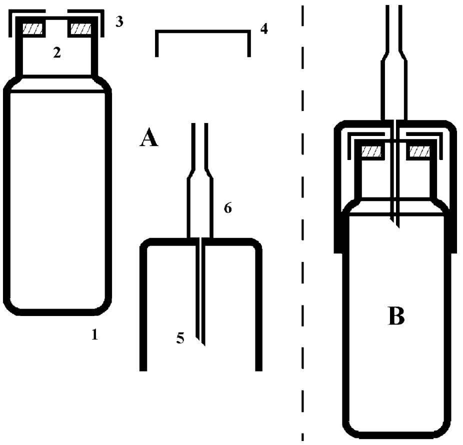

Fig. 1. Jug and hollow needle for sampling tritiated water, *A*: detail, 1: jug, 2: supple rubber membrane, 3: open screwed cork, 4: closed screwed cork, 5: hollow needle, 6: needle guide head, B: jug assembled for sampling the tritiated water.

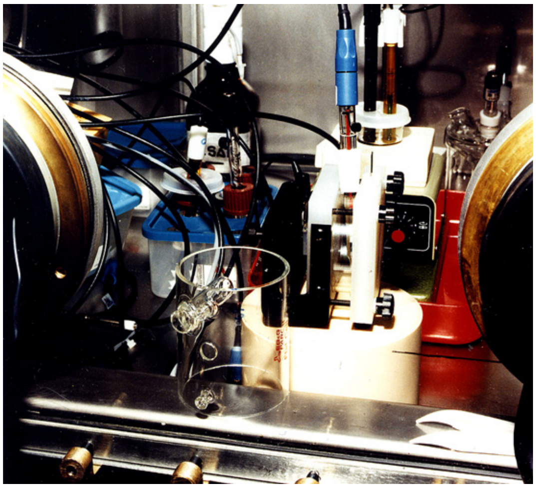

Fig. 2. Electrochemical cell for corrosion tests in glove box.

in a glove box in a ‘hot’ laboratory due to the radiological and contamination risks. The volume of tritiated water used in the cell was 10 cm^3 and its concentration was 3 g dm^{-3} (~2.5% in tritium). To carry out these tests, we have, consequently, radiochemically and chemically analyzed the tritiated water. The tritium concentration in the water was determined with a liquid scintillation spectrophotometer (Beckman LS 1800) and a scintillation fluid (Ultima Gold XR Packard Instruments) as well as with an isothermal microcalorimeter (Setaram c-80) working in the microwatt range. The versatility of this technique has been enhanced by the insertion of miniaturized analytical sensors into the vessel, thus improving the interpretation of the results. Depending on the initial concentration of hydrogen peroxide, chloride and pH, the amounts of these species and nitric acid were added to reproduce their higher concentrations found in tritiated water. High concentration of hydrogen peroxide is usual in close containers for stocking. The concentrations are easily quantified by potentiometric titration and measurements using platinum, chloride-selective and pH electrodes. Potentiometric titration is an oxidation–reduction method where the end-point is indicated by a rapid change in the potential. Hydrogen peroxide was reduced by electrolytic reduction, where the effect of chloride was studied alone. Corrosion tests were realized by polarization technique, cyclic voltammetry, and electrochemical impedance spectroscopy. The electrochemical equipment consisted of a Radiometer bipotentiostat and a signal generator (PRT-20 and GSTP3) connected to a Tektronic 2230 numerical oscilloscope to display the currents in cyclic voltammetry. After storage in the oscilloscope, the curves were recorded on a Hewlett-Packard AXY HP 7440 plotter. The electrochemical impedance diagrams and the polarization curves obtained at a low scan rate were plotted with a Radiometer ZCP 130T generator controlled by a computer monitored by a HP 82324 co-processor. The spectra were obtained in an imposed potentiostatic mode where the current is free to change. The measurement sequence in passivity was (1) to apply a given potential stable within 1 mV to ensure stationary condition to obtain the impedance spectra with good reproductivity, first at the lower temperature, (2) to increase the temperature for the second point of measurement to obtain the next impedance spectra, (3) to repeat the sequence up to the higher temperature. The frequency was scanned from high (100 kHz) to low (10 mHz) frequencies with a sinusoidal voltage variation of ±10 mV. The reference and auxiliary electrodes were saturated calomel (SCE) and platinum electrodes, respectively. A platinum wire was connected to the reference electrode through a 0.1 μF capacitor to eliminate any possible interference and short connection leads were used to minimize inductance effects. The working electrode was mechanically polished using silicon carbide sheets, then with diamond paste down to 1 μm mesh grade before each test. The composition of the stainless steel is given in Table 1. The steel surface was examined after the tests with a Cambridge S90 scanning electron microscope.

Table 1
Composition of 316L stainless steel

Element	Fe	Cr	Ni	Mo	Mn	C
wt%	69	16.8	10.3	2.1	1.4	<0.03

3. Experimental results

3.1. Results obtained with chloride

3.1.1. Polarization and voltammetric curves

The polarization curves obtained with chloride and at a low scan rate of 5 mV s^{-1} are shown in Fig. 3. Two regions

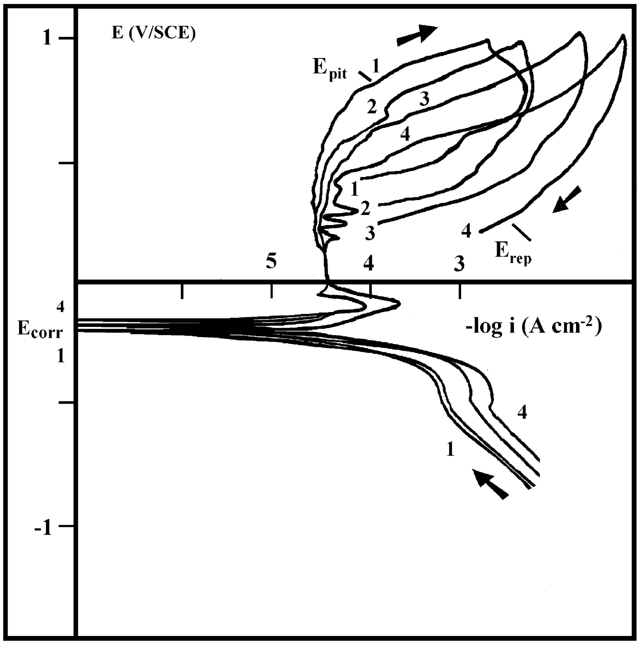

Fig. 3. Polarization curves with chloride, effect of temperature v: 5 mV s^{-1}, A: 0.2 cm^2, pH 4, Cl^-: 5×10^{-2} mol dm^{-3}, temperature: (1) 20; (2) 40; (3) 60; (4) 80 °C.

can be identified: a narrow passive and a large pitting region depending on temperature. The 316L stainless steel remains passivated over a smaller potential domain when the temperature increases. The transition potentials between the pitting potential (E_{pit}) and the repassive potential (E_{rep}) increase with an increase in the temperature. This clearly defines the pitting potential domain and shows that oxide provides protection over the domain located between the prepassivity and the post-prepassivity at high temperature. It can be seen that the corrosion potential (E_{corr}) slightly increases with the temperature, and the small difference between E_{corr} and E_{rep} at the higher temperature should indicate that there is a risk of crevice corrosion.

The use of relatively fast scan rates is unusual in corrosion testing, and the justification for this technique in voltammetry is given by Morris and Scarberry [5]. With the rapid-scan, tests are more sensitive and it is easier to find peaks and inflections whereas in the slow-scan curves, current variation suggests they exist. In addition, during high scan rates, the kinetics of transients can operate differently. Tests realized by cyclic voltammetry at a scan rate of 200 mV s^{-1} (Fig. 4) show the active peak and changes in the pitting current visible only in the return scan on varying the temperature. This corresponds to metastable pitting events. These tests allow us to define the evolution of the critical potentials for pitting and repassivation (Table 2) for a given temperature and to compare the results at different temperatures. As suggested by the shape of the positive hysteresis, pits would continue to initiate and grow in the backward scan up to the potential where the current is zero. At lower potentials than −0.1 V/SCE, the oxides begin to reduce. According to high scan rates, the kinetics in pitting and repassivation are fast (depending on time as seen in the rapid-scan). With regard to curve 4 (Fig. 4), the surface corrodes in places, repassivates by filling the pits at a potential lower than 0.1 V/SCE, consequently there is no pitting propagation in the active and post-active regions at high temperature.

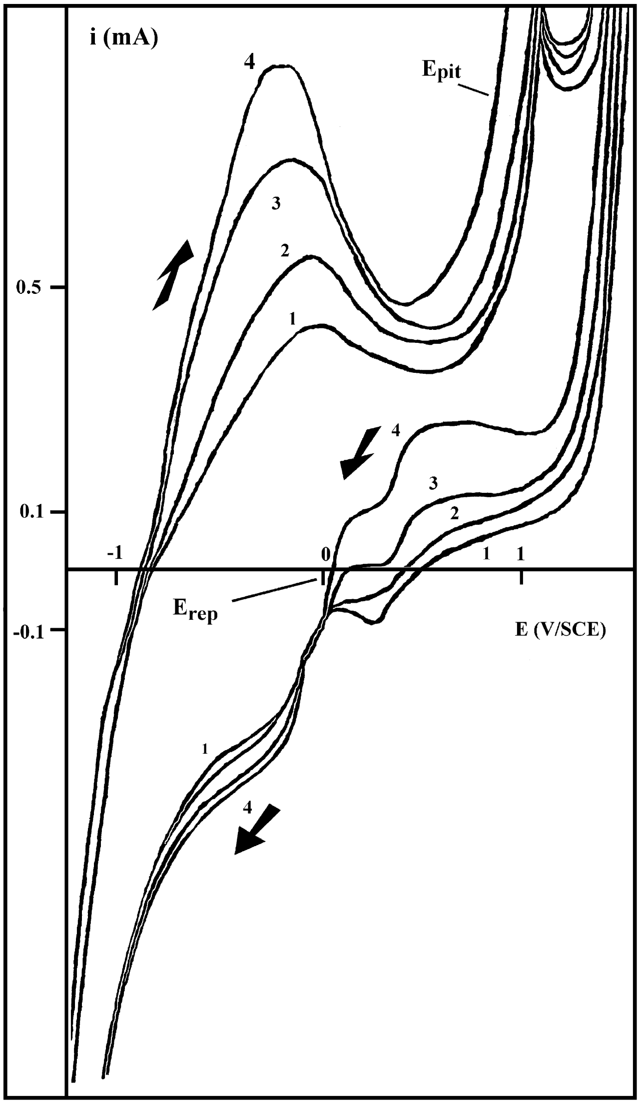

Fig. 4. Voltammetry curves with chloride, effect of temperature v: 200 mV s^{-1}, A: 0.2 cm^2, pH 4, Cl$^-$: 5×10^{-2} mol dm^{-3}, temperature: (1) 20; (2) 40; (3) 60; (4) 80 °C.

Table 2
Pitting and repassivation potentials as a function of temperature with chloride

T (°C)	20	40	60	80
E_{pit} (V/SCE)	0.80	0.74	0.67	0.60
E_{rep} (V/SCE)	0.50	0.35	0.20	0.05

3.1.2. Impedance diagrams

The experimental Nyquist plots obtained for the 316L stainless steel subjected to different temperatures and drawn at the limit of the passive-pitting potentials for each temperature are shown in Fig. 5. A well-defined capacitive semicircle is observed in the spectra at high frequencies. This is the characteristic of charge transfer impedance. This semicircle is followed by an inductive loop at lower frequencies. The inductive loop should be associated with relaxation processes in the oxide layer as indicated by Keddam et al. [6]. It would appear that the chloride ions adsorb and diffuse into the oxide before pitting. In these diagrams, the size of the capacitive semicircle and the aspect of inductive loop depend on the temperature. It can be deduced that the impedance is reduced as the spectrum passes from low to high temperatures. At low temperature, the inductive loop is complete and adsorption is more important, whereas at high temperature, the loop is not entire and pitting is more propagating. The capacitive and inductive regions are delimited by a time constant interacting with the two regions, this is equal to $\tau = \omega_{\mathrm{c}}^{-1}$ where ω_{c} is the characteristic angular frequency separating the semicircle and the loop. To provide physical significance for these spectra and obtain values of electrical circuit, an equivalent circuit is proposed in Fig. 6. In this circuit, the total impedance (Z) will be given by

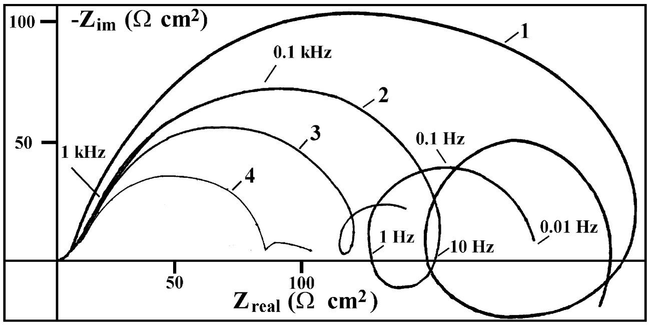

Fig. 5. Nyquist plots with chloride, effect of temperature at the limit of passive-pitting potentials, A: 0.2 cm^2, pH 4, Cl^-: 5×10^{-2} mol dm^{-3}, temperature: (1) 20 °C and 0.675 V/SCE; (2) 40 °C and 0.575 V/SCE; (3) 60 °C and 0.475 V/SCE; (4) 80 °C and 0.425 V/SCE.

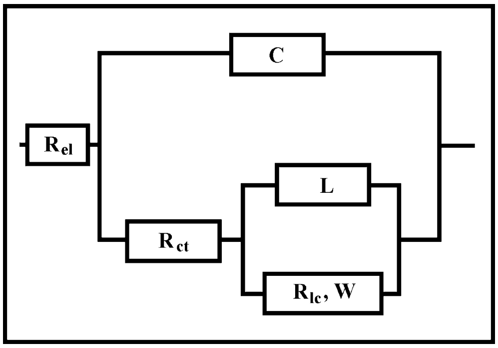

Fig. 6. Equivalent circuit for impedance simulation R_{el}: electrolyte resistance, R_{ct}: charge transfer resistance, C: capacitance, R_{lc}, W: localized corrosion or oxide resistance and Warburg impedance for limited diffusion, L: inductance.

$$1/Z = 1/R_{el} + j\omega C + 1/Z_F, \tag{10}$$

where the faradaic impedance (Z_F) is

$$Z_F = R_{ct} + \frac{j\omega R_{lc}}{j\omega L + R_{lc}}. \tag{11}$$

Here ω is the angular frequency, j is the imaginary operator, R_{ct} is the charge transfer resistance, C reflects an capacitance, R_{el} is the electrolyte resistance, R_{lc} and L are the oxide and corrosion resistance and the inductance implied in the adsorption phenomenon. Suitable values of the circuit elements and the time constant were obtained by calculation using the Circelec program (Table 3). The charge transfer resistance decreases when the temperature increases; this indicates an increase of pitting corrosion. The inductance and time constant values are higher and lower, respectively, when adsorption phenomena are produced at low temperature, and there is an inverted behavior in their values when adsorption is followed by more pitting. The onset of pitting–repassivation can be determined by considering the Eqs. (10) and (11), the limiting value of Z_F for $j\omega \rightarrow 0$ is equal to the repassivation resistance given as R_{ct} in Table 3.

Table 3
Dependence of charge transfer resistance, inductance and time constant on temperature with chloride

T (°C)	20	40	60	80
R_{ct} (Ω cm^2)	190	140	115	85
L (H cm^2)	10	7	4	1
τ (s)	8×10^{-3}	4.2×10^{-2}	0.21	1.7

3.2. Results obtained with hydrogen peroxide

3.2.1. Anodic polarization curves

Anodic polarization curves obtained for different temperatures are presented in Fig. 7. These curves exhibit different characteristics. The corrosion potential is shifted in the passive region where the diffusion of O^{2-} is feasible in the oxide [7]. At the corrosion potential, the corrosion should occur at the cathodic and anodic free sites at acid pH by the following reactions and in the presence of a native oxide which is difficult to reduce at these potentials as shown in Fig. 4 and in [8]. Effectively with regard to this figure, applying an upper potential higher than −0.1 V/SCE did not reduce the native oxide completely.

Cathodic sites:

$$\begin{aligned}&(1+x)^3H_2O_2 + 2(1+x)e^- \\ &\quad \rightarrow x^3H_2O + 2O^3H^- + xO^{2-}_{ads}\end{aligned} \tag{12}$$

where x is the coverage in native oxide. Hydrogen peroxide should be reduced on this oxide.

The cathodic current in the above reaction is

$$i_c = -2(1+x)k_cF[^3H_2O_2]^{(1+x)} \exp -FE/RT. \tag{13}$$

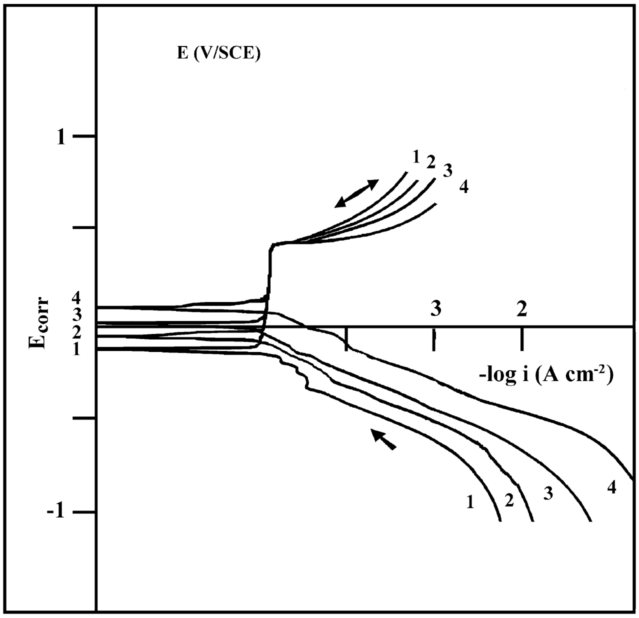

Fig. 7. Polarization curves with hydrogen peroxide, effect of temperature v: 5 mV s^{-1}, A: 0.2 cm^2, pH 4, $^3H_2O_2$: 7×10^{-3} mol dm^{-3}, temperature: (1) 20; (2) 40; (3) 60; (4) 80 °C.

Anodic sites where coverage by the adsorbed species acts for the determining reaction:

$$\mathrm{Me} + 2{}^3\mathrm{H_2O} \rightarrow \mathrm{Me(O^3H)_{ads}} + {}^3\mathrm{H_3O^+} + \mathrm{e^-} \tag{14}$$

$$\mathrm{Me(O^3H)_{ads}} \leftrightarrow \mathrm{MeO^3H^+_{ads}} + \mathrm{e^-} \tag{15}$$

$$\mathrm{Me(O^3H)_{ads}} + {}^3\mathrm{H_3O^+} \leftrightarrow \mathrm{Me^{2+}_{ads}} + 2{}^3\mathrm{H_2O} + \mathrm{e^-} \tag{16}$$

$$\mathrm{MeO^3H^+_{ads}} + {}^3\mathrm{H_3O^+}\mathrm{Me^{2+}_{ads}} + 2{}^3\mathrm{H_2O} \tag{17}$$

$$\mathrm{Me^{2+}_{ads}} + 4{}^3\mathrm{H_2O} \rightarrow \mathrm{Me(O^3H)_2} + 2{}^3\mathrm{H_3O^+} \tag{18}$$

The reaction scheme shows two paths with three intermediates ($\mathrm{Me(O^3H)_{ads}}$, $\mathrm{MeO^3H^+_{ads}}$ and $\mathrm{Me^{2+}_{ads}}$) and one divalent passivating species ($\mathrm{Me(O^3H)_2}$) as shown in [9]. The dissolution through Eqs. (15) and (17) is a fast electrochemical step, but dissolution is controlled by surface coverage through the limiting chemical step (Eq. (18)) and in the presence of limiting electronic diffusion by $\mathrm{O^{2-}}$ in the remaining native oxide, which determine the overall reaction rate when the corrosion potential is in passivity as proposed by Lorenz et al. for a weakly acidic medium [10]. The anodic current for the corrosion potential will be in the free sites as

$$i_\mathrm{a} = k_\mathrm{a}\mathrm{F}\left[\mathrm{Me(O^3H)_{ads}}\right]\left[{}^3\mathrm{H_3O^+}\right]\exp \mathrm{FE/RT}. \tag{19}$$

In Eqs. (13) and (19), k_a and k_c are the anodic and cathodic reaction rate constants (mol cm^{-2} s^{-1}). k_a is governed by Eqs. (15) and (17) but this is controlled by the coverage in hydroxide (Eq. (18)) with ionic diffusion in the native oxide by $\mathrm{O^{2-}}$. $\mathrm{Me(O^3H)_2}$ contributes to passivity by means of an oxide–hydroxide. Therefore, the oxide layer has a complicated chemical structure which is described as a bilayer model. The structure of the related layers changes with the potential, the chemical media and with other factors such as the temperature. These equations show that $\mathrm{O^3H^-}$ and ${}^3\mathrm{H_3O^+}$ are produced and consumed in cathodic and in anodic sites resulting in local pH modifications at the surface of the steel as demonstrated by the previous work in our laboratories [11]. This model where the corrosion potential is in passivity depends on $\mathrm{Me(O^3H)_2}$ and the adsorbed species, but in this region of potential, the point defect model proposed by Macdonald [7] and the simple activation control anodic reactions model coexist and govern all the processes and currents. The corrosion potential of this system is the potential at which both the cathodic and the anodic currents are equal. Measurements of the free potential indicate that this is set around the corrosion potential and the active region when hydrogen peroxide is alone. Therefore these potentials serve as a reference to interpret the results for a nuclear installation where the potential is free. From the previous equations, the simplified expression of E_corr is assumed to be

$$E_\mathrm{corr} = \frac{1.15RT}{\mathrm{F}}\left\{\log\left(\frac{2(1+x)k_\mathrm{c}}{k_\mathrm{a}}\right) + \log\left[{}^3\mathrm{H_2O_2}\right]^{(1+x)} - \log\left[\mathrm{Me(O^3H)_{ads}}\right] + \mathrm{pH}\right\}. \tag{20}$$

Table 4
Corrosion potential of 316L stainless steel as a function of temperature with hydrogen peroxide

T (°C)	20	40	60	80
E_corr (V/SCE)	−0.09	−0.04	0.01	0.06

In this equation, the corrosion potential not only depends on ${}^3\mathrm{H_2O_2}$, pH, the coverage by $\mathrm{Me(O^3H)_{ads}}$, the ratio of the cathodic and anodic reaction rate constants, and the temperature, but also on the $\mathrm{Me(O^3H)_2}$ presence and the native oxide not completely reduced for these potentials. In the experimental conditions, the concentrations of ${}^3\mathrm{H_2O_2}$ and pH are defined and the value estimated is 1.85. Therefore, variation of the corrosion potential with the temperature can be written as

$$\frac{\partial E_\mathrm{corr}}{\partial T} = 10^{-4}\left\{1.85 + \log\left(\frac{2(1+x)k_\mathrm{c}}{k_\mathrm{a}}\right) - \partial\log\left[\mathrm{Me(O^3H)_{ads}}\right]\right\}. \tag{21}$$

The effect was experimentally checked over 20–80 °C and the results are given in Table 4. From the table, we see that $\partial E_\mathrm{corr}/\partial T$ is constant and the value is about 2.5 mV/°C. This result indicates that in Eq. (21), $\mathrm{Me(O^3H)_{ads}}$ is not a second variable, and thereby the electrochemical reactions are controlled by the limiting chemical step (Eq. (18)) and the limiting covering oxide with ionic diffusion of $\mathrm{O^{2-}}$. In Fig. 7, the cathodic and anodic experimental Tafel slopes are about −120 and 74 mV per decade. The large cathodic slope value indicates that the reaction of hydrogen peroxide reduction is limited by diffusion of $\mathrm{O^{2-}}$ in oxide as shown by Nogami and Shiratsuchi [12]. This signifies that the oxide is passivated with ${}^3\mathrm{H_2O_2}$ and that value of the corrosion potential is dependent on its presence and that of native oxide covering the surface. The passive domain is smaller at high temperature.

3.2.2. Voltammetric curves

Fig. 8 illustrates the voltammograms obtained at different temperatures. It can be seen that the presence of hydrogen peroxide significantly affects 316L stainless steel oxidation and reduction processes. The curves exhibit the following characteristics:

(a) in the forward scan, the active peak at −0.2 V/SCE has disappeared and the current takes a negative value when the temperature is high enough. During the backward scan, a major reduction current occurs near −0.5 V/SCE. These negative currents increase with the temperature and correspond to the hydrogen peroxide reduction following the cathodic reaction (Eq. (12)),

(b) the anodic curves intersect the potential axis at more positive potentials with the increasing temperature. At intermediate temperatures, the corrosion potential or the rest potential will be in the active peak and in the active–passive transition (Flade potential). This corresponds to mixed electrode behavior bringing about instabilities in the formation of the oxide layer, which will be more difficult to stabilize and passivate,

(c) at higher temperatures, the passive current partially disappears. The oxide layer is formed in a shorter potential range with the reduction of hydrogen peroxide. Consequently the corrosion potential and the rest potential are in the passive region and the 316L stainless steel should be protected against corrosion in this short domain,

(d) the post-passive region is followed by a transpassive peak preceding the oxide layer dissolution and oxygen evolution potentials. The current increases quickly in this region with high temperature. The reaction concerning dissolution in the transpassive region is

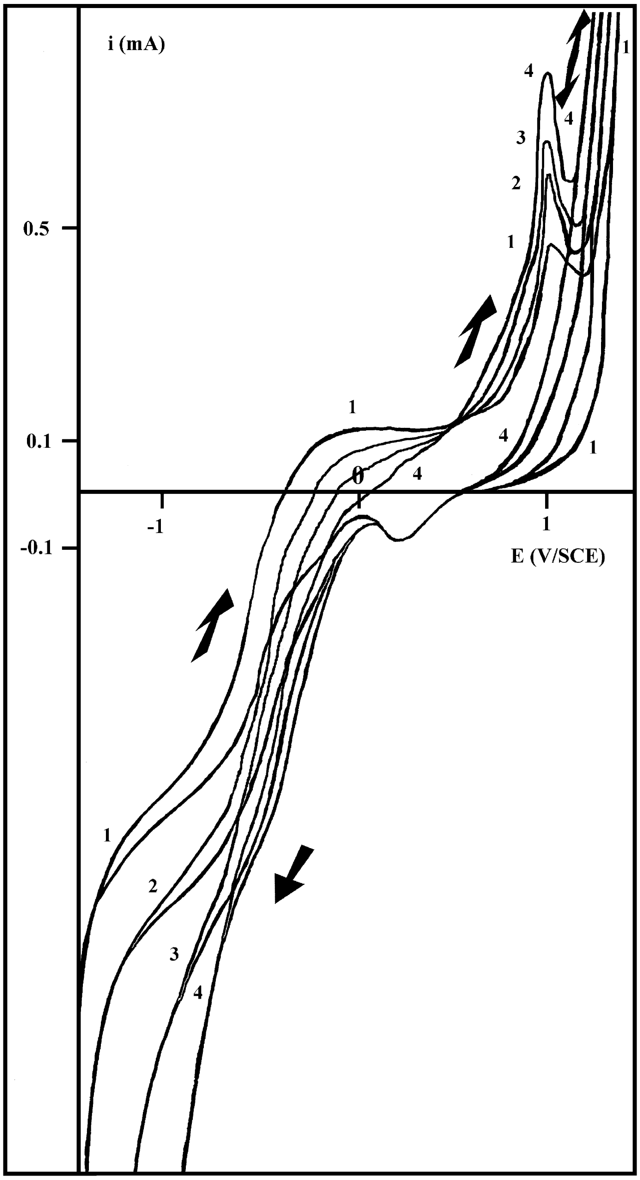

Fig. 8. Voltammetry curves with hydrogen peroxide, effect of temperature v: 200 mV s^{-1}, A: 0.2 cm^2, pH 4, $^3H_2O_2$: 7×10^{-3} mol dm^{-3}, temperature: (1) 20; (2) 40; (3) 60; (4) 80 °C.

$$Me_2O_3 + 3\,^3H_2O_2 + 3\,^3H_2O \rightarrow 2MeO_4^{2-} + 4\,^3H_3O^+ \qquad (22)$$

From this equation, $^3H_2O_2$ participates in the production of acidity with transpassive corrosion.

Evidently high temperature significantly affects all oxidation and reduction processes in limiting the region of passivity by the displacement of the active region in this region. Consequently, the net corrosion current remains in passivity and is equal to the sum of two currents with opposite signs: the current due to 316L stainless steel oxidation at the free sites, according to Eqs. (14)–(18), and the current due to the reduction of $^3H_2O_2$ on the native oxide. To conclude, the corrosion potential and the rest potential are in passivity following the coexistence of two models: the simple activation control anodic reaction model and the point defect model.

3.2.3. Impedance spectra

This section is concerned with the analysis of impedance data for the 316L stainless steel at different temperatures, in the presence of $^3H_2O_2$ and in the region slightly over the corrosion potential, where passive oxide forms. The impedance data will be compared to evaluate the effect of temperature on the oxide and its physical characteristics. Comparative Nyquist plots in Fig. 9 show two distinct regions:

(a) In the high and middle frequency range (1 kHz to 10 Hz), the Nyquist plots exhibit a semicircle. This is the response of the charge transfer resistance. This aspect of the spectra indicates that 316L stainless steel becomes predominantly less resistive in the shorter concerned passive region at high temperature.

(b) In the low frequency range, the diagrams display a tongue which disappears at the higher temperature. This is the characteristic response of adsorption phenomena of hydroxide beside the native oxide.

According to these results, the impedance response may be attributed to two possible consecutive processes in the common active and passive regions: oxide layer adsorption with relaxation at lower temperatures and corrosion followed by protection at higher temperatures. Therefore, the method is suitable for showing the characteristics of oxide, and indicates that the oxide layer obeys a law depending on the parameters: temperature and hydrogen peroxide. This aspect of the Nyquist diagrams indicates more resistive oxide at low and intermediate temperatures, and oxide thickening at high temperature by the decreasing resistance. This reflects, in reality, the formation of a protective oxide layer at high temperature.

One of the aims of plotting the experimental diagrams is to find the values of the main electrical elements using the Circelec software program [13,14]. Diagnostic criteria for the choice of the equivalent circuit for modeling impedance data may be summarized by visual observation of the shifts in the simulated spectra in comparison to the experimental

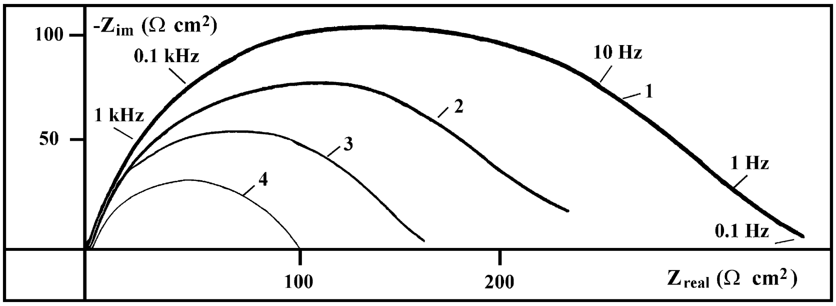

Fig. 9. Nyquist plots with hydrogen peroxide, effect of temperature A: 0.2 cm^2, pH 4, $^3H_2O_2$: 7×10^{-3} mol dm^{-3}, temperature: (1) 20 °C and −0.1 V/SCE; (2) 40 °C and 0.04 V/SCE; (3) 60 °C and 0.09 V/SCE; (4) 80 °C and 0.14 V/SCE (potentials in the active–passive region).

Nyquist plots in changing temperature. In the active–passive region, the spectra give a perfect fit with the experimental data if the total impedance is modeled according to the circuit in Fig. 6. The main values obtained for the electrical elements are given in Table 5. It can be seen that the charge transfer resistance varies from 310 to 100 Ω cm^2. The resistance in this table denotes a behavior due to dissolution in the active region according to Eq. (17) before protection.

To interpret the previous experimental results, it is necessary to adapt the theory of the point defect model in passivity proposed by Macdonald [7] and Lorenz et al. [15] with the simple activation control anodic reaction model taking the valency of two for Me at the tritiated water–oxide interface described as $\mathrm{Me(O^3H)_2}$. Thus, it is easier to understand the adsorption and diffusion controlled processes within the oxide layer and where the corrosion potential is in passivity. The point defect model contains the following basic features:

- the oxide layer contains vacancies (V_{Me}^{n+} and V_{O}^{2-}),
- the vacancies are in equilibrium at the hydrogen peroxide–oxide and oxide–alloy interfaces,
- the oxide layer kinetics and intermediates are governed by vacancies across the oxide layer.

Table 5
Dependence of charge transfer resistance on temperature with hydrogen peroxide

T (°C)	20	40	60	80
R_{ct} (Ω cm^2)	310	220	160	100

Based on these considerations, in combining the point defect model in passivity with the simple activation control anodic reaction model by $\mathrm{Me(O^3H)_2}$, the following reactions, besides Eqs. (12), (14)–(18), are in equilibrium at each interface:

$$\left.\begin{aligned}&\mathrm{Me} \leftrightarrow \{\text{oxide}\} + V_{\mathrm{O}^{2-}} && \text{(23a)}\\ &\mathrm{Me} + V_{\mathrm{Me}^{n+}} \leftrightarrow \{\text{oxide}\} && \text{(23b)}\end{aligned}\right\}\ \text{alloy–oxide interface,} \qquad (23)$$

$$\left.\begin{aligned}&V_{\mathrm{O}^{2-}} + {}^3\mathrm{H_2O_2} + 2\mathrm{e}^- \leftrightarrow {}^3\mathrm{H_2O} + \mathrm{O}^{2-} && \text{(24a)}\\ &\{\text{oxide}\} + 4{}^3\mathrm{H_2O} \leftrightarrow V_{\mathrm{Me}^{n+}} + \mathrm{Me(O^3H)_2} + 2{}^3\mathrm{H_3O^+} + 2\mathrm{e}^- && \text{(24b)}\end{aligned}\right\}\ \text{oxide–hydrogen peroxide interface,} \qquad (24)$$

where {oxide} represents metal cations in the oxide layer which are in equilibrium with the metal cation vacancies. V_{O}^{2-} are produced at the oxide–alloy interface and consumed at the hydroxide–hydrogen peroxide interface in increasing acidity. As a result, V_{O}^{2-} diffuses from the oxide–alloy to oxide–hydrogen peroxide interfaces, or equivalently, O^{2-} diffuses from hydroxide–$^3H_2O_2$ to oxide–alloy interfaces. Similar arguments show that V_{Me}^{n+} diffuses from the oxide–hydrogen peroxide to alloy–oxide interfaces, and equivalently, {oxide} diffuses in the opposite direction. The net results of V_{O}^{2-} migration can be written by combining Eqs. (23a) and (24a):

$$\mathrm{Me} + {}^3\mathrm{H_2O_2} + 2\mathrm{e}^- \leftrightarrow \{\text{oxide}\} + {}^3\mathrm{H_2O} + \mathrm{O}^{2-} \qquad (25)$$

Similarly, combining Eqs. (23b) and (24b) shows that the net result of V_{Me}^{n+} migration can be expressed as

$$\mathrm{Me} + 4{}^3\mathrm{H_2O} \leftrightarrow \mathrm{Me(O^3H)_2} + 2{}^3\mathrm{H_3O^+} + 2\mathrm{e}^- \qquad (26)$$

From the set of previous reactions, it is clear that the diffusion of V_{O}^{2-} (or equivalently O^{2-}) results in oxide thickening and is produced with the consumption of $^3H_2O_2$ at the oxide–hydrogen peroxide interface, whereas the diffusion of V_{Me}^{n+} (or equivalently {oxide}) is accompanied by the formation and adsorption of $\mathrm{Me(O^3H)_2}$ as seen in the active region. The reactions occurring within the oxide are influenced by the different potential drops in the alloy–oxide and oxide–hydrogen peroxide interfaces and with the oxide layer, where the latter is $\Delta\phi$. Therefore, these require field-assisted ion and electron transports through the oxide layer. Within the oxide layer thickness of some tenths of nanometres, the electrical field strength is of the order of some hundreds of mV [16], which enables the migration of ions through the oxide layer at a measurable level in currents of a few µA. This low current enables to limit the current of hydrogen peroxide reduction, thereby the simple activation model controls the anodic reaction on the free sites when the active potentials are in passivity, showing the complexity of the system. According to the point defect model, the oxide–hydrogen peroxide interface is polarizable, therefore it is expected that the total potential drop is a function of oxide layer characteristics, interfacial ${}^3H_2O_2$ concentration and temperature:

$$\partial\Delta E = \partial\Delta E_{\text{oxide–alloy}} + 2.3\frac{R\partial T}{2F}\left[\partial\log\left[{}^3H_2O_2\right]_{\text{interface}}\right] + \partial\Delta\phi, \tag{27}$$

where ΔE represents a potential drop between the interfaces and within the oxide layer. In this equation, the effect of high temperature is similar to that of an increase in the ${}^3H_2O_2$ concentration. Large potential drop may indicate large thickness of the oxide layer with modification of vacancies diffusion and their accumulation at the interfaces up to a critical value depending on potential, temperature and species presence. Critical potential combined with the effects of hydrogen peroxide and temperature will be explained in the next section. In reality, there is large thickness when the point defect model and the simple activation control anodic reaction model are in the passive region for higher temperatures.

3.3. *Results obtained with chloride and hydrogen peroxide*

3.3.1. *Polarization and voltammetric curves*

The polarization curves obtained at different temperatures are shown in Fig. 10. The passive potential domain does not exist as the corrosion potential shifts towards more positive values and the pitting potential shifts very slightly towards lower values at high temperature. Effect on the value of pitting potential is indeed less important in the presence of hydrogen peroxide and at different temperatures than that obtained with the chloride alone. The smaller or negative difference between the corrosion potential and repassivation potential makes it possible to obtain crevice corrosion at higher temperatures. These results imply that chloride and high temperature lead to less O^{2-} vacancies and more metal cation vacancies in passivity as will be seen in the subsequent discussion (Eqs. (30) and (31)). In consequence the oxide layer will be defective and will not provide protection, and the number of pits and crevices would increase in this oxide by chloride and hydrogen peroxide at high temperature. From scanning micrographs (Fig. 11), it is seen that the 316L stainless steel is highly corroded over all the surfaces with crevices, pitting and generalized corrosion.

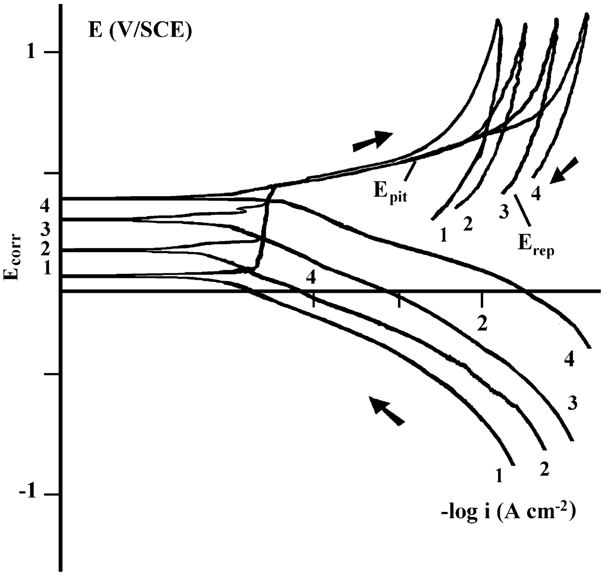

Fig. 10. Polarization curves with chloride and hydrogen peroxide, effect of temperature v: 5 mV s^{-1}, A: 0.2 cm^2, pH 4, Cl^-: 5×10^{-2} mol dm^{-3}, ${}^3H_2O_2$: 7×10^{-3} mol dm^{-3}, temperature: (1) 20; (2) 40; (3) 60; (4) 80 °C.

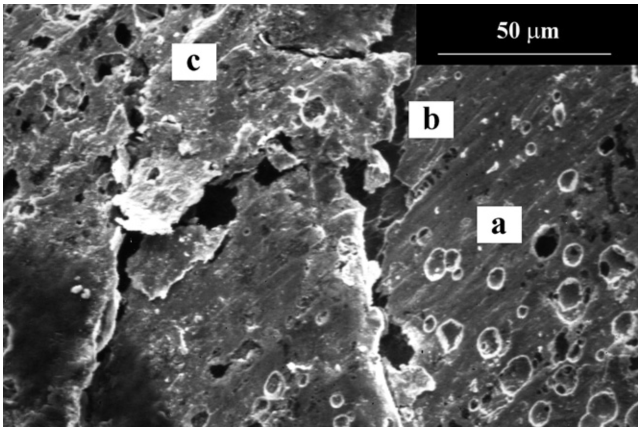

Fig. 11. Scanning electron microscopy of 316L stainless steel (a) pits, (b) crevices, (c) generalized corrosion, in presence of 5×10^{-2} mol dm^{-3} Cl^- and 7×10^{-3} mol dm^{-33}H_2O_2, at 0.45 V/SCE, temperature: 80 °C.

In the voltammetric curves (Fig. 12), it can be seen that the current in the active peak is shifted towards more negative values. This type of current results from the ${}^3H_2O_2$ reduction current superimposed on the active corrosion current. An increase in the temperature leads to an increase in the pitting currents in the forward and backward scan. In this context, pitting is aided by the displacement of corrosion potential towards the passive–transpassive region with increasing temperature. According to the aspect of the curves (small difference between the corrosion potential and the repassivation potential and high currents), crevice corrosion is feasible. No current fluctuations are seen, the kinetics of oxide layer breakdowns and localized corrosion are so fast that these are not observable.

To interpret the experimental results obtained with chloride and hydrogen peroxide at different temperatures, it is

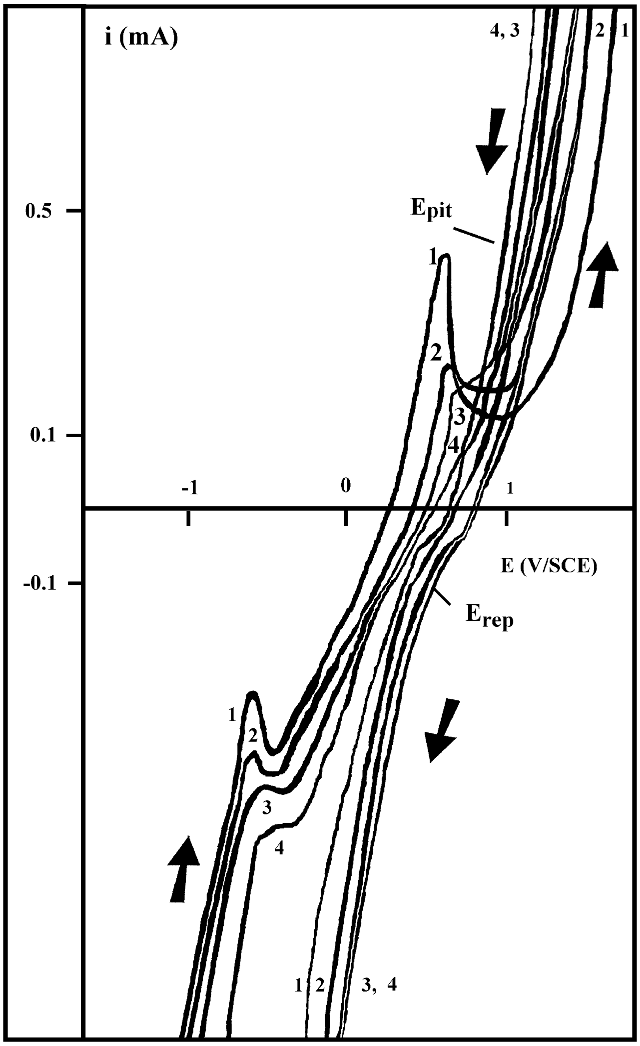

Fig. 12. Voltammetry curves with chloride and hydrogen peroxide, effect of temperature v: 200 mV s^{-1}, A: 0.2 cm^2, pH 4, Cl$^-$: 5×10^{-2} mol dm^{-3}, $^3H_2O_2$: 7×10^{-3} mol dm^{-3}, temperature: (1) 20; (2) 40; (3) 60; (4) 80 °C.

useful to use the theory of the point defect model within the chloride diffusion model. According to Strehblow [16] and Macdonald [7,17], if the metal cation vacancies penetrate the alloy at a slower rate than their diffusion through the oxide layer, they accumulate at the alloy–oxide layer interface and finally lead to a local concentration and hence will form a void. When the void grows to a certain critical size, the oxide layer suffers local collapse, which then marks the end of the pit incubation period when chlorides are present. The collapsed site dissolves much faster than any other location on the layer, thereby leading to pit growth. From this, the diffusion of metal cation vacancies is affected by adsorption and the incorporation of Cl$^-$ ions at the oxide–$^3H_2O_2$ interface as shown in the following equations:

$$V_{\mathrm{Me}}^{n+} - \frac{n}{2}V_{\mathrm{O}^{2-}} = 0 \tag{28}$$

$$C_{V_{\mathrm{Me}}^{n+}} = k(C_{V_{\mathrm{O}^{2-}}})^{-0.5n} \tag{29}$$

$$V_{\mathrm{O}^{2-}} + \mathrm{Cl}^-_{\text{aqueous-ads}} \leftrightarrow \{\mathrm{Cl}^-\} \tag{30}$$

Eq. (28) represents the Schottky-pair reaction at the oxide–$^3H_2O_2$ interface. In Eqs. (29) and (30), {Cl$^-$} is a chloride anion occupying O^{2-} vacancies and C is the vacancies concentration with an inverse dependence on V_{Me}^{n+} and V_{O}^{2-}. It can be seen that the number of free V_{O}^{2-} vacancies decreases in the presence of chloride. Inversely, due to interdependence of the concentration of cation and anion vacancies and the adsorption and diffusion of Cl$^-$ within the oxide layer, as shown by ellipsometry [18], the number of metal cation vacancies increases in the oxide layer up to a critical concentration leading to localized corrosion at the pitting potential. From these considerations, the criterion for pit initiation in the presence of $^3H_2O_2$ can be expressed with the rate of diffusion in oxide and/or by the variation of incubation time of chloride which can be estimated from $\Delta(E_{\mathrm{pit}} - E_{\mathrm{corr}})$ in the polarization curves (Fig. 10).

$$\frac{\partial V_{\mathrm{Me}^{n+}}}{\partial t} = J_{\mathrm{o}}\left[C_{V_{\mathrm{O}^{2-}}}\{\text{oxide} - {}^3\mathrm{H_2O_2}\}\right]^{-0.5n} \tag{31}$$

In this equation giving the diffusion rate in oxide, J_{o} depends on thermodynamic constants and $C_{V_{\mathrm{O}^{2-}}}\{\text{oxide–}{}^3\mathrm{H_2O_2}\}$ is the concentration of O^{2-} vacancies at the oxide layer–$^3H_2O_2$ interface. Eq. (31) signifies that the metal cation vacancies diffusion is enhanced by decreasing the concentration of O^{2-} vacancies, e.g., with chloride present and/or by a small incubation time when its adsorption and diffusion are fast. This enhancement can effectively lead to the accumulation of metal cation vacancies at the alloy–oxide layer interface. From Eqs. (28) and (31), and applying a calculation procedure similar to that given by Strenblow [16] and Macdonald et al. [7,17], the simplified equation in the presence of $^3H_2O_2$ and Cl$^-$ and for different temperatures can be written as

$$E_{\mathrm{cri}} = \frac{4.6RT}{\alpha Fn}\log\left(\frac{J_{\mathrm{m}}}{J_{\mathrm{o}}\frac{M}{\rho}\exp\left\{\frac{{}^3\mathrm{H_2O_2}}{RT}\right\}^{-0.5n}_{\text{interface}}}\right) - \frac{2.3RT}{\alpha F}\log \mathrm{Cl}^-, \tag{32}$$

where E_{cri} is the potential for critical collapsing, J_{m} is the rate of submergence of the metal cation vacancies in the alloy, M is the mean molar weight of oxide, n the mean number of electrons required to form the oxide and ρ the oxide density. From this equation, it can be seen for high submergence rates, that the temperature combined with chloride (second term in Eq. (32)) shifts the pitting potential towards less positive values, thereby favoring pitting. It can also be deduced that temperature combined with hydrogen peroxide (first term in Eq. (32)) acts in contrary on the pitting potential. Therefore, in Eq. (32), the temperature has two effects that are inverted with regard to hydrogen peroxide and chloride, and these would validate the experimental results since the displacement of pitting potential is very low in Fig. 10. These also confirm the results in the curves obtained with chloride alone (Fig. 3), and the potential of the passive–transpassive transition in the curves obtained with hydrogen peroxide alone (Fig. 7). Therefore, temperature combined with hydrogen peroxide acts for passivity. But, temperature with hydrogen peroxide will be indirectly dangerous in the sense, that it displaces the corrosion potential towards the repassivity region making possible crevice corrosion at high temperature possible.

3.3.2. Electrochemical impedance spectroscopy

The experimental Nyquist plots obtained for the 316L stainless steel subjected to a constant concentration for Cl^- and $^3H_2O_2$ and for different temperatures are shown in Fig. 13. Changes in the temperature affect the position of frequency and the size of the partial or complete capacitive semicircle suggesting mass transport. In these Nyquist diagrams, the inductive loop, visible with chloride or hydrogen peroxide alone, should be hidden by the resistive and the capacitive effects. Along the capacitive semicircle, the total impedance is predominantly resistive over a broad frequency range, while the capacitive part is predominant only for higher frequencies where the semicircle is incomplete at low frequencies. On increasing the temperature, the decrease in size of the partial capacitive semicircle suggests pitting and crevice processes in agreement with Figs. 10–12. In order to account for these observations, $^3H_2O_2$ reduction participating in oxide formation and localized corrosion processes leading to pitting take place simultaneously and are enhanced with the temperature. The experimental diagrams can be satisfactorily explained on the basis of the equivalent circuit approach presented in Fig. 6 where the adsorption inductance corresponding to the MeO^3HCl_{ads} and $Me(O^3H)_2$ formation [1] has a small effect in comparison to the pitting and crevice processes. The values of the equivalent circuit elements are given in Table 6. Data in this table indicate that the charge transfer resistance is very low and the capacitance, estimated from $C = (\pi f_c R_{real})^{-1}$ where f_c is the characteristic frequency at the top of the semicircle, is unusually high (more than 160 $\mu F\ cm^{-2}$). The capacity value does not correspond to a double layer or an oxide layer capacitance (~50 and 5 $\mu F\ cm^{-2}$, respectively). This indicates high localized corrosion with pitting and crevice corrosion. Comparison of the electrical resistance values with those given in Tables 3 and 5 indicates that for the same temperature, oxide layer is less protected with chloride and hydrogen peroxide, signifying more important localized corrosion.

Table 6
Dependence of charge transfer resistance on temperature with chloride and hydrogen peroxide

T (°C)	20	40	60	80
R_{ct} ($\Omega\ cm^2$)	47	36	27	21

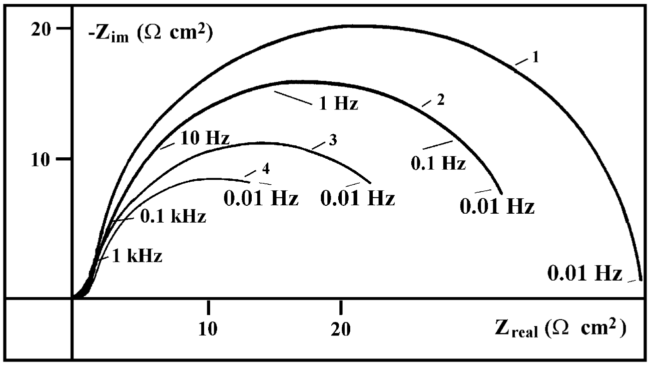

Fig. 13. Nyquist plots with chloride and hydrogen peroxide, effect of temperature A: 0.2 cm^2, pH 4, Cl^-: 5×10^{-2} mol dm^{-3}, $^3H_2O_2$: 7×10^{-3} mol dm^{-3}, temperature: (1) 20; (2) 40; (3) 60; (4) 80 °C and 0.42 V/SCE.

In order to model the adsorption on the oxide with hydrogen peroxide and chloride, we have numerically analyzed and carried out calculations to obtain the characteristics, the size and the structural aspect of the adsorbed species in the presence of hydroxonium ions using the Chem-Office™ program. During the last years, considerable effort has been made on solving the structure of the adsorbed layers. Achievement in this field is well illustrated by a handbook containing a catalogue of these structures [19] and database can be obtained using a graphic program [20]. As an example, the structures of MeO^3HCl_{ads}, O^{2-}, $\{Cl^-\}$ and $Me(O^3H)_2$ linked to $MeO^3H^+_{ads}$ are shown in Fig. 14. This figure schematizes the well-ordered complexes adsorbed on the oxide layer. As schematized in Fig. 14, these species produce a radioligand layer, and the considered surface and volume have been modeled, the adsorbed layer lying in parallel to the oxide surface in order to get a reasonable coverage. In this model, $^3H_3O^+$ ions bonded to

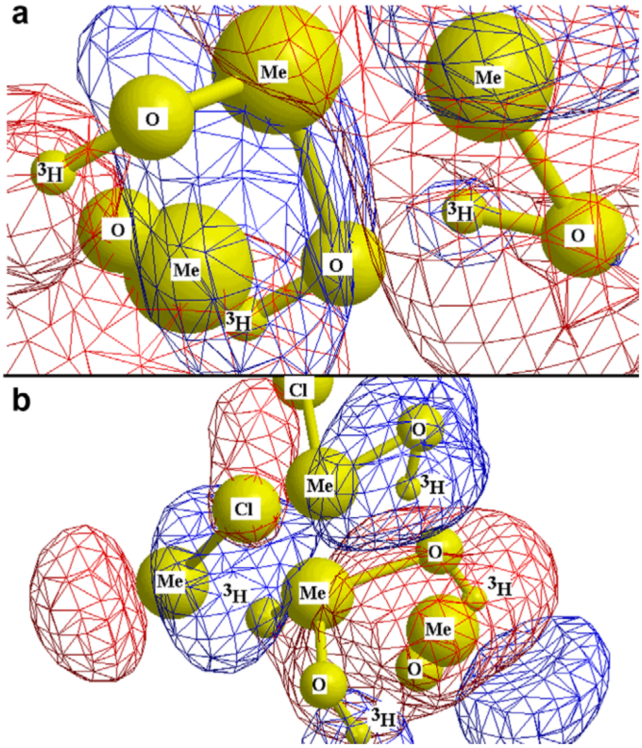

Fig. 14. Structure in 3D dimension of $Me(O^3H)_2$, $MeO^3H^+_{ads}$ and MeO^3HCl_{ads} in presence of $^3H_3O^+$ ions (a) without MeO^3HCl_{ads} species, (b) with MeO^3HCl_{ads} species.

Table 7
Bond lengths, angles, closer contact between species, orbital size of adsorbed species ($Me(O^3H)_2$, $MeO^3H^+_{ads}$ and MeO^3HCl_{ads}), ionic radius and size of $^3H^+$ and $^3H_3O^+$

	Bond lengths (nm)			Angles (°)	Orbital (nm)
	$O–^3H$	Me–O	Me–Cl	$Me–O–^3H$	
$Me(O^3H)_2$, $MeO^3H^+_{ads}$	0.17–0.27	0.15	–	67	1.25
MeO^3HCl_{ads}	0.41	0.29	0.26	14	0.83
Closer contact (nm)	Me/O	0.1	Ionic radius $^3H^+$ (nm)		0.15
	Me/Cl	0.09	$^3H_3O^+$ size (nm)		0.4
	$O/^3H$	0.14			

the anionic species participate in ionization. MeO^3HCl_{ads} overlaps the adjacent adsorbed hydroxides and fills the different orbitals. Calculations using the MerckIndex™ database give the bond lengths and angles for these different species in minimizing energy and take into account the $^3H_3O^+$ ions. Results are reported in Table 7. In this table, it can be seen that the bond angles, the bond lengths and orbitals of $Me(O^3H)_2$ and $MeO^3H^+_{ads}$ differ to those obtained with MeO^3HCl_{ads} presence. MeO^3HCl_{ads} has the tendency to increase the bond lengths of hydroxide radicals. Increasing these bond lengths decreases the bond and adsorption strengths, and consequently the corresponding driving force is less important than that obtained when $Me(O^3H)_2$ and $MeO^3H^+_{ads}$ are alone. It can be deduced that the chloride limits the adsorption of hydroxide and thereby diffusion of O^{2-}. Diffusion of O^{2-} favors oxide growth.

4. Conclusion

For safety reason and to avoid contamination, special sampling of tritiated water and the design of electrochemical cell are presented and explained. The 316L stainless steel subjected to tritiated water containing chloride, hydrogen peroxide at acid pH and at different temperatures shows a well defined localized corrosion region over a wide range of potentials going from the corrosion potential to transpassivity. Two influences are simultaneously observed during the increase in temperature: a high cathodic current corresponding to hydrogen peroxide reduction aiding oxide formation, and a high anodic current corresponding to a strong corrosion by pitting and crevice attack by chloride. In this context, the corrosion potential is in the limit of passivity–transpassivity when the temperature is high enough. This produces more localized corrosion accompanied by generalized corrosion at acid pH. It can also be thought that chloride and hydroxide formed by hydrogen peroxide reduction lead to adsorption and diffusion into oxide, facilitating the overlap of the active and localized corrosion regions at high temperature. According to our results obtained by electrochemical analysis methods and scanning electron micrography, increasing the temperature facilitates defective oxide formation and pitting and crevice corrosion. The 316L stainless steel is highly corroded in tritiated water containing chloride, hydrogen peroxide at acid pH and high temperature.

References

[1] G. Bellanger, Corrosion Induced by Low-Energy Radionuclides – Modeling of Tritium and its Radiolytic and Decay Products Formed in Nuclear Installations, Elsevier, Amsterdam, 2004.

[2] A. Bruggeman, M. Snykers, P. de Regge, Fus. Technol. 14 (1988) 828.

[3] W.G. Burns, P.B. Moore, Radiat. Eff. Def. 30 (1976) 233.

[4] J.K. Linacre, W.R. Marsh, Report R 10027, Chemistry Division, Atomic Energy Research Establishment, Harwel, 1981.

[5] P.E. Morris, R.C. Scarberry, Corrosion 26 (1970) 169.

[6] M. Keddam, in: P. Marcus, J. Oudar (Eds.), Corrosion Mechanisms in Theory and Practice, M. Dekker, New York, 1995, p. 55.

[7] J.R. Macdonald, Impedance Spectroscopy, J. Wiley, New York, 1987.

[8] G. Bellanger, J.J. Rameau, J. Mater. Sci. 35 (2000) 1759.

[9] I. Epelboin, C. Gabrielli, M. Keddam, H. Takenouti, in: J. O'M Bockris, B.E. Conway, E. Yeager, R.E. White (Eds.), The Study of the Passivation Process by the Electrode Impedance Analysis, Plenum, New York, 1981, p. 151.

[10] A.A. El Miligy, D. Geana, W.J. Lorenz, Electrochim. Acta 20 (1975).

[11] G. Bellanger, J.J. Rameau, J. Nucl. Mater. 228 (1996) 24.

[12] G. Nogami, R. Shiratsuchi, J. Electrochem. Soc. 140 (14) (1993) 919.

[13] J.P. Diard, P. Landaud, B. Le Gorrec, C. Montella, in: C. Gabrielli (Ed.), Deuxième Forum sur les Impédances Electrochimiques, University P.M. Curie, Paris, 1987.

[14] J.P. Diard, B. Le Gorrec, S. Maximovitch, Electrochim. Acta 35 (1990) 1099.

[15] J.B. Bessone, D.R. Salinas, C.E. Mayer, M. Ebert, W.J. Lorenz, Electrochim. Acta 37 (12) (1992) 2283.

[16] H.H. Strehblow, in: P. Marcus, J. Oudar (Eds.), Corrosion Mechanisms in Theory and Practice, M. Dekker, New York, 1995, p. 201.

[17] C.Y. Chao, L.F. Lin, D.D. Macdonald, J. Electrochem. Soc. 128 6 (1981) 1194.

[18] C.L. McBee, J. Kruger, R.W. Staehle, et al. (Eds.), Localized Corrosion, NACE, Houston, 1974, p. 252.

[19] J.M. McLaren, J.B. Pendry, P.J. Rous, D.K. Saldin, G.A. Somorjai, M.A. Van Hove, D.D. Yvedensky, Surface Crystallographic Information Service – A Handbook of Surface Structure, Reidel, Dordrecht, 1987.

[20] J.B. Pendry, Surface Crystallographic Information Service – Data Base and Graphics Programs, Riedel, Dordrecht, 1987.